Institute Report
IB 111-2005/34

The vortex trajectory method applied to HART II PIV data

Frauke Hoffmann
Berend G. van der Wall

Braunschweig, Germany

44 Pages with
11 Tables,
17 Figures and
6 Literatures

Level of access: I - unlimited distribution.

German Aerospace Center (DLR)
Institute of Flight Systems
Helicopter Division
Lilienthalplatz 7, D-38108 Braunschweig

Braunschweig, August 25, 2005

Signatures:

Head of Institute:	Prof. Dr.-Ing. S. Levedag	_____
Head of Division:	Dipl.-Ing. J. Pausder	_____
Author:	Dipl.-Ing. F. Hoffmann	_____
Author:	Dipl.-Ing. B. G. van der Wall, MS.	_____

Contents

List of Figures

List of Tables

Notation

Abbreviations

AS	Advancing Side
BL	Baseline
CS	Coordinate System
DNW	German-Dutch Wind tunnel
Dpt	Data point
HART	HHC Aeroacoustic Rotor Test
HHC	Higher Harmonic Control
LLF	Large Low-speed Facility
MN	Minimum Noise
MV	Minimum Vibration
PIV	Particle Image Velocimetry
Pos	Position
RS	Retreating Side
SPR	Stereo Pattern Recognition
WT	Wind Tunnel

Symbols

r	$[m]$	radial coordinate
R	$[m]$	rotor radius
x, y, z	$[m]$	coordinates
α	$[°]$	angle of attack
β_p	$[°]$	pre-cone angle
ψ	$[°]$	azimuth angle

Indices

el	elastic
hub	rotor hub
$trav$	traverse
$view$	view
V	vortex
0	origin

1 Introduction

In October 2001 the HART II test campaign took place in the LLF of the DNW. During this test, data of 1TB were acquired including extensive wake data for the advancing and retreating side of the rotor plane. In the scope of this campaign, three test cases were distinguished: BL, MN and MV. 3C-PIV measurements were conducted to understand vortex roll up in the rotor wake as well as vortex aging in order to develop advanced simulation tools.

A test matrix as illustrated in Fig. 1 has been used to gather data for the reference blade vortex at different ages. To avoid disturbances due to blade presence, PIV data have been taken at two different azimuths of $\psi = 20°$ and $\psi = 70°$ for advancing and retreating side.

PIV windows have been focused on vortex centers and cover a cross section of $0.46m \times 0.37m$ for DNW and $0.15m \times 0.13m$ for DLR windows. The smaller DLR cross section is caused by a different camera lense and thus associated with a higher spatial resolution than the resolution provided by the DNW windows. Looking from the top to the measurement set-up, PIV windows are rotated by $\psi_{PIV} = -30.43°$ for the advancing and $\psi_{PIV} = +30.06°$ for the retreating side. In the following these angles of the PIV windows are simplyfied to be $\psi_{PIV} = \pm 30°$ regarding to the different sides of the rotor plane.

Due to the orientation of the PIV windows, most of them are cut by the vortices almost perpendicular which is important for correct analysis of the circumferential flow field of them. However global vortex structures are 3D-systems and an inclination of the vortex axis of unkown magnitude with respect to the measurement plane is always present. In Fig. 2 a vortex cutting the PIV measurement plane is shown. The PIV plane is inclined by the angles β_x and β_z referring to the plane that is created perpendicular to the vortex axis. To obtain flow field data normal to the vorex axis, the PIV window has to be rotated by β_x and β_z.

Due to the huge amount of data gained during the HART II test, an automatic tool for analyzing vortex characteristics has been developed in the past. The implemented algorithm identifies the rotation angles from the velocity field of the data. This method is based on the assumption that the cross-flow parallel to the vortex axis is homogenous. Another method for the computation of β_x and β_z is provided by determining vortex center locations in space and connecting them by polynomials representing vortex trajectories. The rotation angles β_x and β_z then are given by the inclination angle at the vortex centers. In the following, the first method is called the cross-flow method while the latter one is referred to as trajectory method.

In this report the computation of β_x and β_z using the trajectory method is explained and in the following the results are presented and compared to the results of the cross-flow method.

2 Transformation of vortex center coordinates

2.1 Definition of coordinate systems and their origins

For each blade vortex its position for different vortex ages has to be determined. Vortex positions are represented by the vortex center coordinates wich are identified by the automatic analyzing tool as detailed described in [1] and [2]. For a presentation of the rotor wake with respect to the rotor hub system, vortex centers given in PIV window coordinates have to be transformed accordingly. Therefore, coordinate systems as summerized in Tab. 1 are introduced following the order of transformation. Fig. 3 shows a schematical illustration of the different coordinate systems and their positioning to each other.

Wind tunnel coordinate system. The wind tunnel coordinate system is used as reference system with its origin located 7m downstream of the nozzle exit on the tunnel center line. The x_{WT} axis is defined postive downstream, the y_{WT} axis positive to the right, looking upstream. The z_{WT} axis is defined positive upwards.

PIV coordinate system. The PIV coordinate system is specified individually for each data point with its according PIV window. The origin of the PIV system is located in the vicinity of the centerpoint of the PIV window. The y_{PIV} axis is specified positive in the direction of sight of the PIV cameras (Fig. 3). The x_{PIV} axis always is defined positive to the right also with respect to the camera viewing direction. Consequently, it is oriented positive against the direction of flow at the advancing and positive in the direction of flow for the retreating side. The z_{PIV} axis as the rotation axis is defined positive upwards.

Rotor hub coordinate system. For the case that the shaft angle of attack is equal to zero (shaft axis vertical, tip path plane horizontal), the hub center is positioned 70mm upstream of the origin of the wind tunnel system and 915mm above this point as illustrated in Fig. 4. The hinge of the sting support for varying the angle of attack is located 4400mm downstream and 174.5mm below the tunnel center line.

Since the angle of attack of the model is varied by the sting, for each α-variation a horizontal displacement in the $x_{hub,WT,0}$ coordinate of the rotor hub position is resulting while the coordinates $y_{hub,WT,0}$ and $z_{hub,WT,0}$ for the origin of the coordinate system do not change. Assuming the support from α-hinge to the model to be infinitely stiff, the centerpoint of the rotor hub in wind tunnel coordinates depending on the angle of attack α can be computed as follows

$$\begin{pmatrix} x \\ y \\ z \end{pmatrix}_{hub,WT,0} = \begin{pmatrix} 4400mm - 4601mm \cdot \cos(13.7° + \alpha) \\ 0 \\ 915mm \end{pmatrix}_{hub,WT,0} \quad (1)$$

The $x_{hub,WT}$ axis of the rotor hub system is defined positive downstream, the $y_{hub,WT}$ axis positive to the right when looking upstream and the $z_{hub,WT}$ axis positive upwards.

2.2 Vortex center coordinates in the wind tunnel coordinate system

Using PIV window origin positions $(x, y, z)_{trav,WT}$ in the wind tunnel coordinate system and vortex center coordinates $(x, y, z)_{V,PIV}$ in the PIV window coordinate system, the

position of the vortex center in the wind tunnel system can be computed. The vortex center coordinates $(x,z)_{V,PIV}$ are determined from the velocity field of the PIV window. The $y_{V,PIV}$ coordinate is equal to zero because the PIV window plane is defined at $y_{PIV} = 0$.

Fig. 3 illustrates the geometrical relations between PIV and wind tunnel coordinate system. Considering the PIV angle ψ_{PIV}, the vortex center is shifted regarding to the origin of the PIV coordinate system as described in Equ. 2.

$$\begin{pmatrix} x \\ y \\ z \end{pmatrix}_{V,WT} = \begin{pmatrix} x \\ y \\ z \end{pmatrix}_{trav,WT} + \begin{pmatrix} x \cdot \cos\psi_{PIV} \\ x \cdot \sin\psi_{PIV} \\ z \end{pmatrix}_{V,PIV} \tag{2}$$

2.3 Vortex center coordinates in the rotor hub coordinate system

In order to obtain the vortex center positions relative to the rotor hub center, hub center coordinates following Equ. 1 have to be subtracted. The resulting vortex center coordinates are still in axis parallel to the wind tunnel system.

$$\begin{pmatrix} x \\ y \\ z \end{pmatrix}_{V,hub,WT} = \begin{pmatrix} x \\ y \\ z \end{pmatrix}_{V,WT} - \begin{pmatrix} x \\ y \\ z \end{pmatrix}_{hub,WT,0} \quad \text{with } y_{hub,WT,0} \simeq 0 \tag{3}$$

The $(x,y,z)_{V,hub,WT}$ coordinates are employed for the computation of β_z.

In order to obtain trajectories in the view 1,2-perspectives of Fig. 3, which is necessary for the identifcation of β_x, the $(x,y,z)_{V,hub,WT}$ coordinates (without α-rotation) have to be transformed about the view angle $\psi_{view} = \pm 30°$ using Equ. 4. At the advancing side the sense of rotation is negative while it is defined positive for the retreating side. The $z_{V,hub}$ coordinate does not change since the $z_{hub,WT}$ axis is defined as rotation axis.

$$\begin{pmatrix} x \\ y \\ z \end{pmatrix}_{V,view1/2} = \mathbf{T}_{\psi_{view}} \cdot \begin{pmatrix} x \\ y \\ z \end{pmatrix}_{V,hub,WT} \quad \text{with} \quad \mathbf{T}_{\psi_{view}} = \begin{bmatrix} \cos\psi_{view} & \sin\psi_{view} & 0 \\ -\sin\psi_{view} & \cos\psi_{view} & 0 \\ 0 & 0 & 1 \end{bmatrix} \tag{4}$$

At angles of attack $\alpha \neq 0$, the $(x,y,z)_{V,hub,WT}$ coordinates have to be rotated about α since the rotor plane is inclined about the $y_{hub,WT}$ axis by the angle of attack. α-rotated vortex center coordinates $(x,y,z)_{V,hub}$ are needed to analyze vortex flight paths in the rotor plane. The coordinates are computed using the transformation according to Equ. 5 and

$$\begin{pmatrix} x \\ y \\ z \end{pmatrix}_{V,hub} = \mathbf{T}_{\alpha} \cdot \begin{pmatrix} x \\ y \\ z \end{pmatrix}_{V,hub,WT} \quad \text{with} \quad \mathbf{T}_{\alpha} = \begin{bmatrix} \cos\alpha & 0 & -\sin\alpha \\ 0 & 1 & 0 \\ \sin\alpha & 0 & \cos\alpha \end{bmatrix} \tag{5}$$

In the following for all vortex center coordinates referring to the different coordinate systems, the index "V" is omitted.

3 Computation of vortex trajectories

A pre-requisite for the computation of the angles between the PIV measurement plane and the vortex axis, β_x and β_z, is the computation of vortex trajectories in space by connecting vortex center positions of a constant blade azimuth.

3.1 Computation method

The transformation angles β_x and β_z have been computed for all three test cases of the HART II test: BL, MN and MV. Despite of the excistence of counter rotating vortices for the MN and MV case, only blade tip vortices are analyzed for this report. In some cases, counter rotating vortices are used to interpolate vortex center coordinates for missing data points as described in section Sect. 3.2.

After transforming vortex center coordinates into the rotor hub system, they are plotted for the $xy_{hub,WT}$-plane for the β_z calculation and the $xz_{view1/2}$-plane for the calculation of β_x. The vortex center coodinates for different ages of the blade tip vortex then are connected by polynomials which illustrate vortex trajectories appoximated via regression analysis.

For creating polynomials in the $xy_{hub,WT}$-plane using MS Excel, it is necessary to rotate the rotor hub coordinate system counter clockwise by $90°$ plotting the $x_{hub,WT}$ axes versus the $-y_{hub,WT}$ axes. Polynomials representing the according trajectories are given by the functions $x_{hub,WT} = f(-y_{hub,WT})$ in the $xy_{hub,WT}$- and $z_{hub,WT} = f(x_{view1/2})$ in the $xz_{view1/2}$-plane. The functions for the different polynomials are summarized in the Tab. 9 - Tab. 11. Derivatives of the functions at the vortex center locations represent the inclination of the tangent to the polynomial. By computing the $\arctan$ of the inclination the angles γ_x and γ_z are obtained.

$$\gamma_x = \arctan \frac{dz_{hub,WT}}{d(x_{view1/2})} \qquad \gamma_z = \arctan \frac{dx_{hub,WT}}{d(-y_{hub,WT})} \tag{6}$$

As illustrated in Fig. 5(c) and 5(d), γ_x is specified as angle between $x_{view1/2}$ axis and the tangent to the polynomial at the vortex center while γ_z is specified as the angle between the $-y_{hub,WT}$ axis and the tangent to the polynomial, see Fig. 5(a) and 5(b). To determine the transformation angles β_x and β_z, Equ. 7 is derived from the geometrical relations between the angles.

$$\beta_x = \begin{cases} -\gamma_x & \text{AS} \\ \gamma_x & \text{RS} \end{cases} \qquad \beta_z = \begin{cases} -\gamma_z + 30° & \text{AS} \\ \gamma_z - 30° & \text{RS} \end{cases} \tag{7}$$

Since both transformation angles refer to the PIV coordinate system, there is no special order for a rotation about β_x and β_z that has to be followed after. Note, that the sense of rotation for β_x varies depending on the side of the rotor plane.

3.2 Preparation of PIV measurements

Interpolation of data points. As mentioned in Sect. 1, PIV measurements were taken at the two different rotor azimuths of $\psi = 20°$ and $\psi = 70°$. For this report, the azimuth of $\psi = 20°$ was chosen as reference azimuth. In areas where data were only taken at an azimuth of $\psi = 70°$ those are interpolated to the reference azimuth using linear interpolation according to Equ. 8.

$$\vec{x}^* = \vec{x}_1 + \frac{\psi^* - \psi_1}{\psi_2 - \psi_1} \cdot (\vec{x}_2 - \vec{x}_1) \tag{8}$$

The coordinates $\vec{x}_1$ and $\vec{x}_2$ are the two neighboring PIV positions with the missing data point $\vec{x}^*$ laying in between them. As described previously, Fig. 1 illustrates the locations of the PIV windows which are positioned at rotor azimuths of $\psi_1 = 20° + n \cdot 90°$ as well as $\psi^* = 70° + n \cdot 90°$ with $n = 0, 1, 2, 3, 4, 5, 6$ to trace the vortex of the reference blade. In most of the cases the rotor azimuth differences were computed as $\psi^* - \psi_1 = 50°$ and $\psi_2 - \psi_1 = 90°$, such that frequently

$$\vec{x}^* = \vec{x}_1 + \frac{5}{9} \cdot (\vec{x}_2 - \vec{x}_1) \tag{9}$$

To achieve best results in the approximation of vortex trajectories by polynomials, not measured data points were also interpolated from neighbored PIV positions based on Equ. 8.

Estimation of the trajectory starting point. Missing data points in the blade tip area of the rotor plane cannot be interpolated due to missing neighboring data points. By assuming that the blade vortex approximatly is created at the blade tip, the vortex center can be assumed to be located at $r/R = 1$. Based on this assumption, "virtual" vortex center coordinates can be computed related to the blade tip position at the y_{hub} coordinate of interest for the vortex flight path plots, and at the azimuth of interest for the trajectory plots. For the flight path at a given $y_{hub,WT}$:

$$\begin{aligned} x_{hub,WT} &= \sqrt{R^2 - y_{hub,WT}^2} \\ \psi &= arctan(y/x)_{hub,WT} \end{aligned} \tag{10}$$

By calculating the $x_{hub,WT}$ coordinate, the rotor azimuth ψ in the second and third quadrant of the rotor disk is given which is needed for the calculation of the $z_{hub,WT}$ coordinate. For the blade tip with $r/R = 1$ the $y_{hub,WT}$ coordinate for instance is $y_{hub,WT} = -0.4R$ for the retreating side with an according rotor azimuth of $\psi = 203.6°$. For consistency of the data points, the rotor azimuth is assumed to be $\psi = 200°$ which is a multiple of the reference azimuth of $\psi = 20°$ ($200° = 20° + 2 \cdot 90°$) and needed for the trajectory.

Additionally to the rotor azimuth ψ, the vertical blade tip position z_{tip} depends on the pre-cone angle β_p of the rotor.

$$z_{hub,\beta_p} = R \cdot \sin\beta_p \qquad \beta_p = 2.5° \tag{11}$$

Furthermore a deflection due to the elasticity of the rotor blades has to be considered. This deflection depends on the active forces and moments at the blades which are varying with rotor azimuth. Using the rotor azimuth ψ computed above, the elastic flapping position $z_{hub,el}(\psi)$ at the blade tip can be determined from SPR measurements also taken during the HART II test, [3] and [4].

$$z_{tip} = z_{hub,\beta_p} + z_{hub,el}(\psi) \tag{12}$$

Interpolation using CR vortices. For the MN and MV case, another interpolation method based on the excistence of counter rotating vortices is added. In cases where the tip vortex or the center of vorticity was outside the PIV window they often could be estimated from DNW windows of CR vortices, where the structures of interest were also included within the PIV window.

4 Results

Results for the vortex inclination angles β_x and β_z with respect to the PIV measurement plane obtained by cross-flow and trajectory method are presented in App. B. Tables only include comparable data points that were available for both of the computational methods. Interpolated data points only were employed to generate appropriated polynomials and are not listed in the tables.

Depending on the blade tip vortices are generated at, in Fig. 6, Fig. 9, Fig. 13 and Fig. 7, Fig. 10, Fig. 14 vortices are printed in a representing color as summarized in Tab. 2. The vortex color extension "no. 2" shows the vortices created at an azimuth of $\psi = 360°$ previous to the creation of the vortices black, green, blue and red. Interpolated data points are marked by a superscripted *-sign. All data points shown in Fig. 6 - Fig. 15 are plotted at the reference azimuth of $\psi = 20°$. PIV window positions in the wind tunnel are symbolized by black lines centered about the vortex center coordinates, see Fig. 6, Fig. 9 and Fig. 13. The different directions of sight for the computation of β_x are pointed out by arrows in the $xy_{hub,WT}$-plane regarding to advancing (view 1) and retreating side (view 2).

Additionally to the results for β_x and β_z, vortex center coordinates in the xz_{hub}-plane at $y = (0.4, 0.55, 0.7, 0.85, 0.97)R$ for the advancing as well as $y = -(0.4, 0.55, 0.7, 0.85, 0.97)R$ for the retreating side are plotted for all three test cases. This way, vortex flight paths through the rotor plane with increasing age can be tracked. The rotor is represented in the figures by the pure precone assuming the beam to be stiff.

4.1 Baseline case

Results for β_z. Vortex trajectories are very uniform for the BL case such that the vortex center coordinates at the advancing as well as the retreating side can be approximated by one continous polynomial in Fig. 6. The results for β_z computed with the trajectory method are in good agreement with the results obtained from the cross-flow method (Tab. 3). Larger angle differences are computed for the inner positions 6, 7, 8 and 32 as well as the outer positions 52, 53. It seems that for the inner positions of the rotor plane where polynomials have to approximate a large distance without interpolation points, it is difficult to determine reliable results for β_z using trajectories. As visible for position 52 and 53, the use of the trajectory method also can be difficult for end points of the polynomial.

Results for β_x. Fig. 7(a) shows the polynomials obtained for the advancing side, Fig. 7(b) shows them for the retreating side.

A comparison of cross-flow and trajectory method for β_x only shows marginal differences for most of the data points at the retreating side. Larger differences can be seen at the advancing side, especially for end points of the polynomials like position 23 and 27 (Tab. 4).

Vortex flight path. In Fig. 8(a) vortex center coordinates obtained by measurements as well as interpolated coordinates in the xz_{hub}-plane are plotted for different blade vortices at the advancing, in Fig. 8(b) for the retreating side.

In the front of the rotor disk, blade vortices first are moving upwards due to the upwash effect generated by the self-induced velocity in the rotor plane. Additionally vortices are deflected upwards by the rotor shaft that is rotated about the angle of attack $\alpha = 5.3°$. Moving downstream, the flight paths of the vortices increasingly are dominated by the

thrust causing them to move downwards until they are passing the rotor cone in the area of $x_{hub} = 0.5R$ to $0.8R$ at the advancing side. At the retreating side vortices are cutting the rotor cone in the area of $x_{hub} = 0.35R$ to $0.8R$. For both sides of the rotor, the height of the vortex flight paths above the cone is decreasing for outer areas of the rotor plane.

4.2 Minimum noise case

Results for β_z. Polynomials for approximating vortex trajectories become more complex for the MN case. At the retreating side where blade and thus vortex circulation is larger due to smaller dynamic pressure gradients, vortices of strong vorticity are generated and therefore the according trajectories are very uniform. In contrast, vortex flight paths at the advancing side cannot be adapted correctly by continous polynomials, such that they have to be split up in the area of $-y_{hub,WT} \simeq -0.4R$ of the rotor plane (Fig. 9). Due to HHC inputs, the velocity distribution over the rotor blade is changing combined with a change in the lift distribution. As a consequence, CR vortices are generated at the tip and blade vortices are generated at radially inboard locations which causes different flight paths compared to the BL case.

For vortex black no.2 no polynomial could be created. Because of missing data points the positions 14, 22 as well as 15 and 23 only can be connected straight. Therefore, the results for β_z are not given in Tab. 5 and Tab. 6. Results obtained for β_z at the retreating side are in good agreement with the angles determined from the algorithm method. But again the results computed by the trajectory method differ a lot from those obtained by the cross-flow method for inner positions of the polynomials like 31, 32 and 33. At the advancing side mostly end points of the polynomials (22, 23, 26, 27, 30) are available for comparison but here the computed angles are in good agreement with the cross-flow method. Due to the splitting of the polynomials, β_z for position 6 and 7 is determined from the polynomials of the retreating side. But the results for these positions differ a lot from the cross-flow method probably because both positions are end points of the polynomials. Since no measurements are available for position 5 and 13, no comparison of the two methods could be done. Therefore, they are not listed in the tables.

Results for β_x. At the advancing side the trajectories of vortex green no. 2 and vortex red no. 2 are slightly deflected upwards in the outer area of the rotor, see Fig. 10(a). At the retreating side this effect can be seen for vortex blue, black, green no. 2, blue no. 2 and red no. 2 in Fig. 10(b). These deflections are caused by the roll-up tendency of the vortices due to an interaction between them in the outer area of the rotor plane. The differences in the results for β_x determined from the different methods are very large at the advancing side for end points of the polynomials like position 7, 6, 26, and 30, see Tab. 6. At the retreating side the results are in very good agreement with the results obtained by the cross-flow method.

Vortex flight path. For the MN case, also an upward motion can be seen in Fig. 12(a) and Fig. 12(b) before the vortices are moving downwards through the rotor plane passing the cone in the area of $x_{hub} = 0.2R$ to $0.4R$ at the advancing and $x_{hub} = 0.3R$ to $0.7R$ at the retreating side. In comparison to the BL case, the upward motion of the vortices is more flat at the advancing side such that the maximum height is of lower magnitude. As seen for the BL case, again the maximum height above the rotor plane is decreasing for outer areas of the rotor.

In Fig. 11, PIV windows for the determination of the vortex centers are arranged according to their traverse positions in the wind tunnel, exemplarly at $y_{hub} = 0.4R$, in order to track

the vortex flight path in the xz_{hub}-plane. Having a look at the PIV windows, one can recognize that often no clear vortex structure can be found such that the identification of the vortex center coordinates becomes quite difficult. For example, often only a band of vorticity is present (Dpt. 983, 984, 985) in the PIV windows or the vortex was cut by a blade as it can be seen in Dpt. 1005.

4.3 Minimum vibration case

Results for β_z. For the computation of β_z, polynomials again are split up since a continuos polynomial cannot fit the data points in an appropriate way due to the complex vortex trajectories. For the MV case, PIV measurements were also taken for CR vortices that additionally are shown in Fig. 13. Similiar to the MN case, blade vortices are generated more inboard of the rotor plane while the CR vortices are created at the blade tip. In the front of the rotor plane, CR vortices are located ahead of the blade vortices but they are moving faster with increasing age, passing the blade vortices in the rear of the rotor plane (see CR vortex red no. 2, CR cortex green no. 2, CR vortex black no. 2).

The results for β_z are summarized in Tab. 7, the differences to the angles computed by the cross-flow method are shown in Tab. 8. Higher differences for the results of β_z can be seen for the inner positions 31, 32 and 33 and end points of the polynom like position 52 and 53 at the retreating side. For the advancing side the differences in β_z between both methods are of high magnitude for almost all of the comparable positions (6, 19, 21, 30).

Results for β_x. Polynomials for the computation of β_x are shown in Fig. 14(a) for the advancing side and in Fig. 14(b) for the retreating side. At the advancing side almost all comparable positions are end points of the polynomials (position 6, 19, 20, 21 and 30). Therefore, the computed β_x angles strongly differ from the results determined by the cross-flow method. At the retreating side the results are in good agreement for all of the positions, except for end points of the polynomials like position 52 and 53.

Vortex flight path. As seen for the BL and MN case, vortices first are moving upwards and then downwards in the rear area of the rotor plane for the advancing (Fig. 15(a)) as well as the retreating (Fig. 15(b)) side. Vortex flight paths at the retreating side are located very close to each other cutting the rotor cone in the area of $x_{hub} = 0.4R$ to $0.7R$. At the advancing side the passing area is located between $x_{hub} = 0.4R$ and $0.8R$.

5 Verification of the results

For an evaluation of the two different methods for computing the transformation angles β_x and β_z, the results for vortex parameters after a rotation of the velocity vector field of the vortex about β_x and β_z are compared. Therefore, the vortex parameters vorticity ω_y as well as the cross-flow velocity v_y are employed here. An important quality criterion regarding to the vorticity is a rotational symmetric in-plane vector field while the cross-flow velocity should show a homogenous velocity distribution without global gradients.

A comparison and evaluation of the results exemplarly is shown for position 21 and postion 23 of the BL case to point out differences in the results between the two methods as well as difficulties in the application of the trajectory method.

Fig. 16(a) and 16(d) show both parameters in the measurement plane for $\beta_x = \beta_z = 0°$ for position 21. The vorticity seems to be hardly influenced in its vector field by a transformation using β_x and β_z regardless the computation method the angles are determined from (Fig. 16(a)-16(c)).

For the cross-flow velocity, clear differences between the vector field in the measurement plane and the vector fields resulting from the different methods are visible. In Fig. 16(d) a large global gradient for the cross-flow velocity can be seen from top to buttom such that the cross-flow velocity is of postitive magnitude in the upper half of the figure and of negative magnitude in the lower part. The vortex center is marked right on the border between positive and negative velocities. After rotation, in Fig. 16(e) and 16(f)), the global gradients cannot be seen anymore and the scalar distribution of the cross-flow velocity has a much more vortex-like structure with a circular vortex center located in the middle of the maximum velocity values. The shear layer is seen to be rolled around the vortex center (red spiral). Since for position 21 the angles β_x and β_z computed by the different methods are similiar in magnitude, the results for the vector field of the cross-flow velocity as well as the vorticity obtained by the two methods agree with each other.

Fig. 17 shows a comparison of the same parameters for position 23. The results for β_x and β_z computed by the different methods strongly vary in β_x. While in the measurement plane the vorticity is of elliptical shape (Fig. 17(a)) it is rotational symmetric after a rotation about the transformation angles (Fig. 17(b)) computed by the cross-flow method. Using β_x and β_z obtained from the trajectory method the vorticity vector field again is of elliptical shape, see Fig. 17(c).

For the unrotated cross-flow velocity in Fig. 17(d) again a clear visible gobal gradient is present. This swirl contribution also can be seen in Fig. 17(f) after rotating about β_x and β_z calculated by the trajectory method, in terms of positive and negative cross-flow peaks at the core radius. In comparison, a rotation about the angles of the cross-flow method shows more appropriate results since in Fig. 17(e) a homogenous velocity vector field without global gradients can be seen.

As described before, the trajectory method does not provide reliable results for end points of the polynomials. Since position 23 of the BL case is such an end point, differences in the results of the rotation angles compared to those of the cross-flow method are caused by systematics the computation method is based on, as summarized in Sect. 6. As shown for position 21 the trajectory method provides appropriate rotation angles at intermediate points of the trajectories.

6 Conclusion

When vortex trajectories are matched well by polynomial representation, results for the rotation angles β_x and β_z correlate well with the cross-flow analysis method.

An important disadvantage of the trajectory method is given by the high amount of stand-alone data points that cannot be connected by polynomials and thus no rotation angles can be calculated, while the cross-flow analysis method does not have this limitation.

At the end of a polynomial the following vortex trajectory is unknown. For that reason, the gradient of the polynomial cannot be computed well and no reliable transformation angles using the trajectory method can be determined for end points of the polynomial.

Using polynomial representation of vortex trajectories, physical effects in the rotor plane have to be understood since vortex trajectories and therefore the polynomials strongly depend on them. Consequently, a wide à-priori knowledge about these effects is necessary to meet the real vortex trajectories in a physically meaningful way. For the analyzed test cases BL, MN and MV the resulting polynomials highly vary in shape. Thus, it could become difficult to develop an automatical tool for the computation of β_x and β_z based on this method. Often, the fitting has to be done "by hand".

Polynomials are based on data points refering to one reference azimuth but often measurements are taken at different azimuths. Data points not measured at the specified reference azimuth have to be interpolated. To also analyze the interpolated data points, the interpolation process has to be repeated for the azimuth they actually were gathered at. Additionally, also missing data points have to be interpolated to create appropriate polynomials. Due to the high amount of those data, the interpolation process can become very time consuming and cumbersome.

The results for inner points of the polynomials obtained by the trajectory method are in good agreement with the results of the cross-flow method. But for data points at which the transformation angles computed by the different methods vary strongly, the cross-flow method seems to provide better results in terms of the resulting in-plane velocity vector field and the cross-flow distribution as shown examplarily in Sect. 5.

In conclusion, all these limitations do not exist in the cross-flow analysis method, such that this method is to be prefered for future analysis. Anyway, the results of all computational methods must be critically checked for plausibility.

References

[1] B. G. van der Wall, 2^{nd} HHC Aeroacoustic Rotor Test (HART II) - Part I: Test Documentation -, Institute Report IB 111-2003/31, DLR, Braunschweig, 2003

[2] Paper of B. G. van der Wall and H. Richard at the 2005 ERF, Analysis Methodology for 3C PIV Data, 31st European Rotor Forum, Florence, Italy, 2005

[3] B. G. van der Wall, Casey L. Burley, 2^{nd} HHC Aeroacoustic Rotor Test (HART II) - Part II: Representative Results -, Institute Report IB 111-2005/03, DLR, Braunschweig, 2003

[4] O. Schneider, B. G. van der Wall, Completion of SPR Data Analysis from HART II, Report IB 111-2004/07, DLR, Braunschweig, 2004

[5] G. Leishman, Principles of Helicopter Aerodynamics, Cambridge University Press, 2000

A Figures

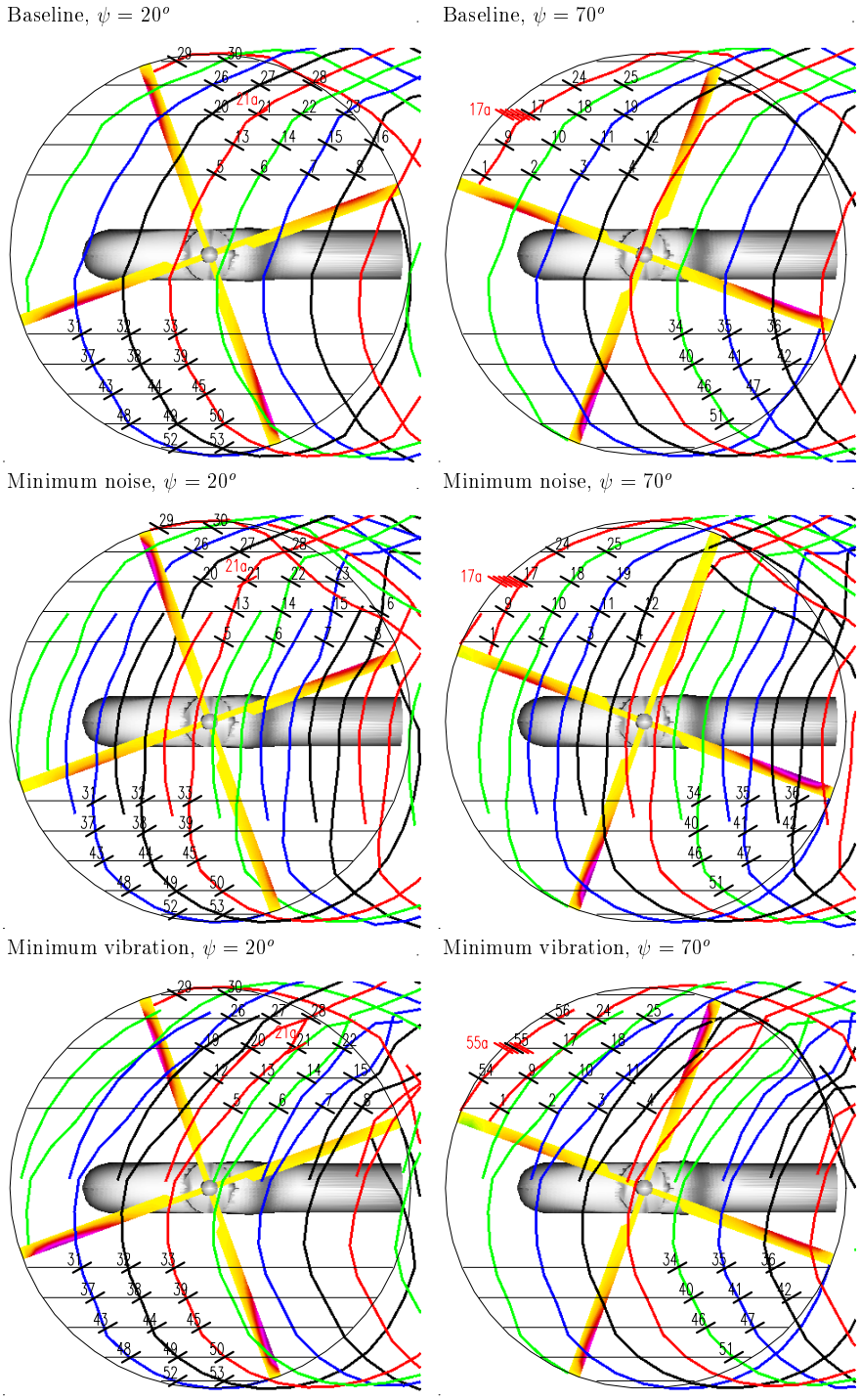

Figure 1: PIV test matrix with position numbering scheme, wind from left

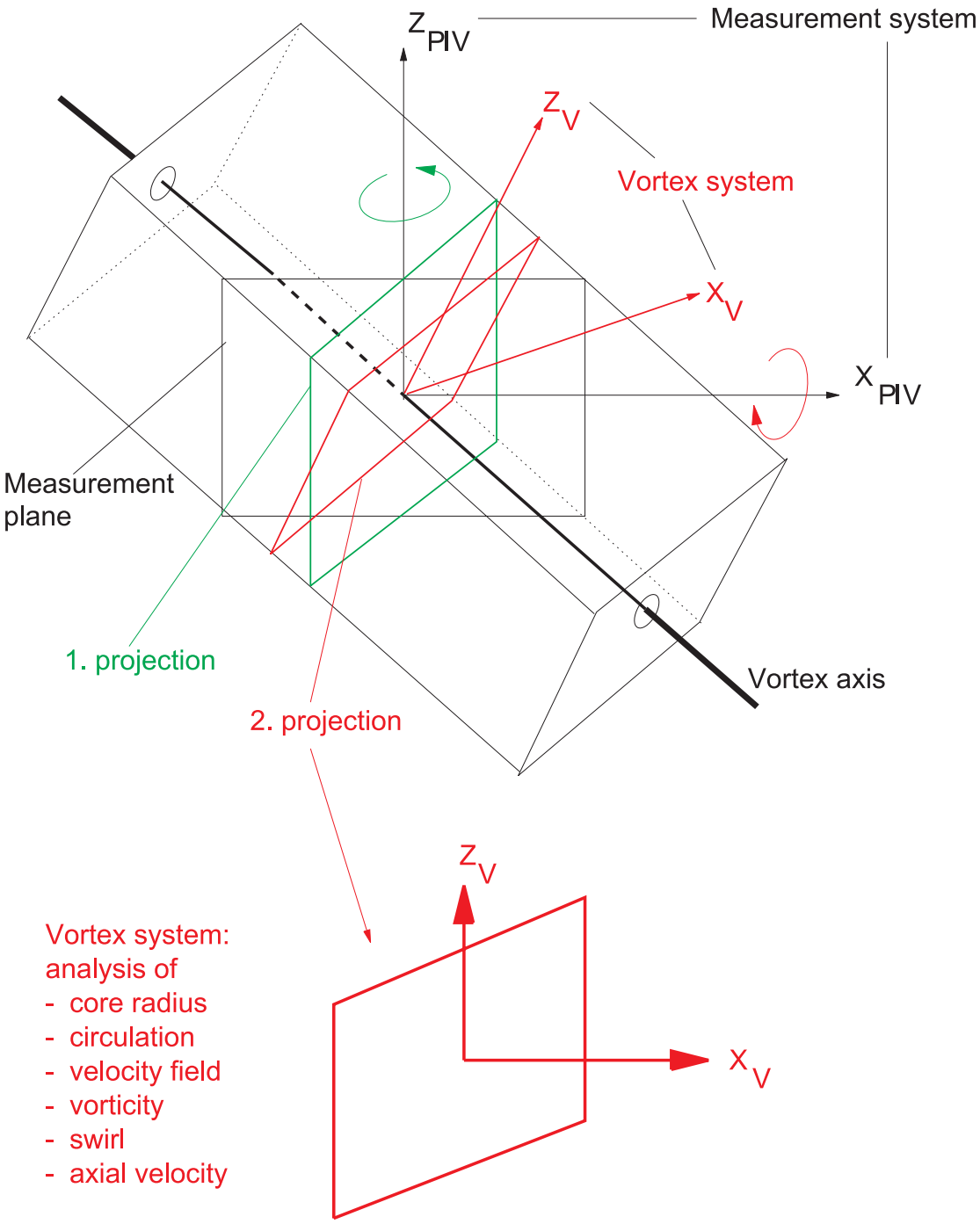

Figure 2: Scheme of transformations from PIV measurement plane into a plane normal to the vortex axis

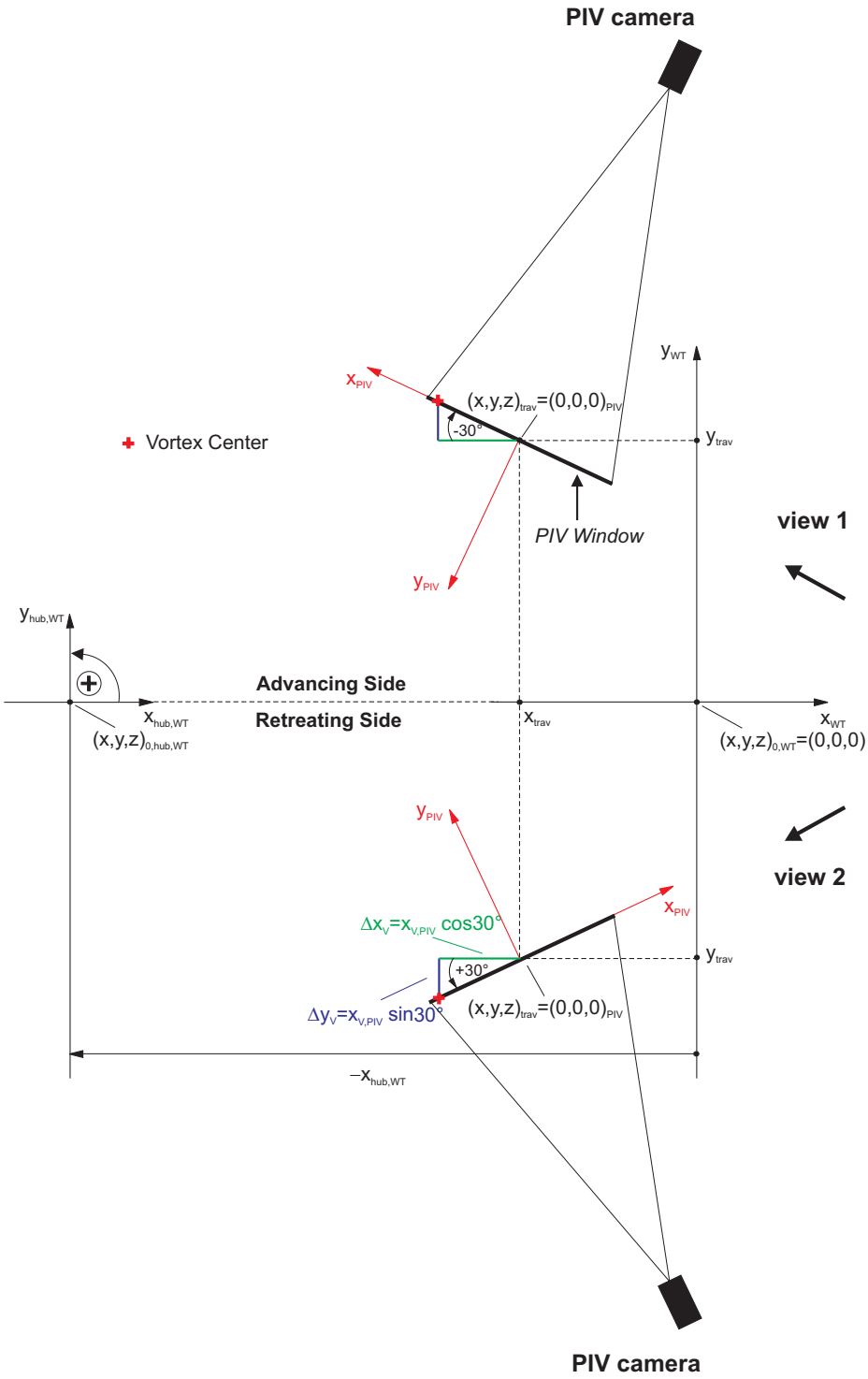

Figure 3: Calculation of vortex center coordinates in the wind tunnel, PIV and rotor hub system

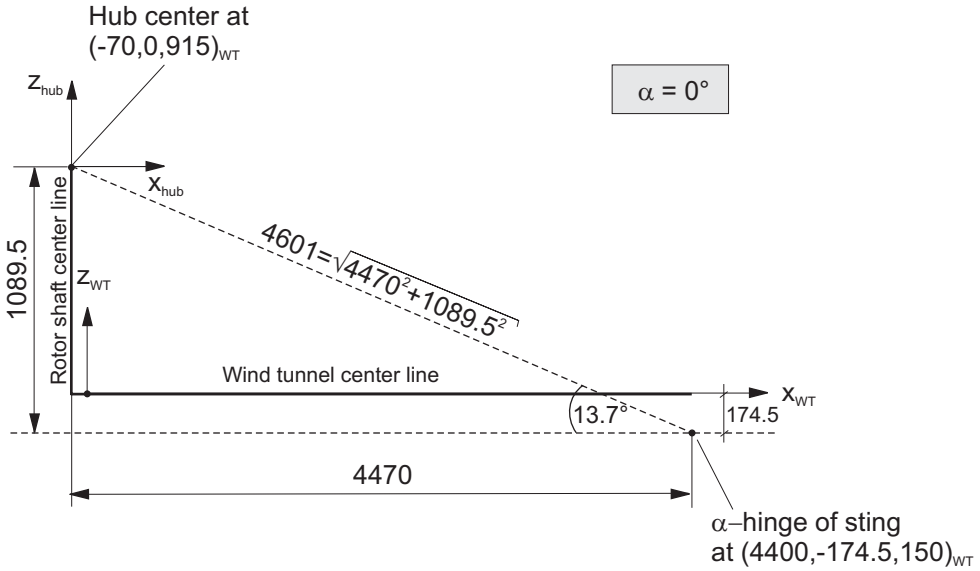

Figure 4: Hub center position in the wind tunnel, all dimensions in mm

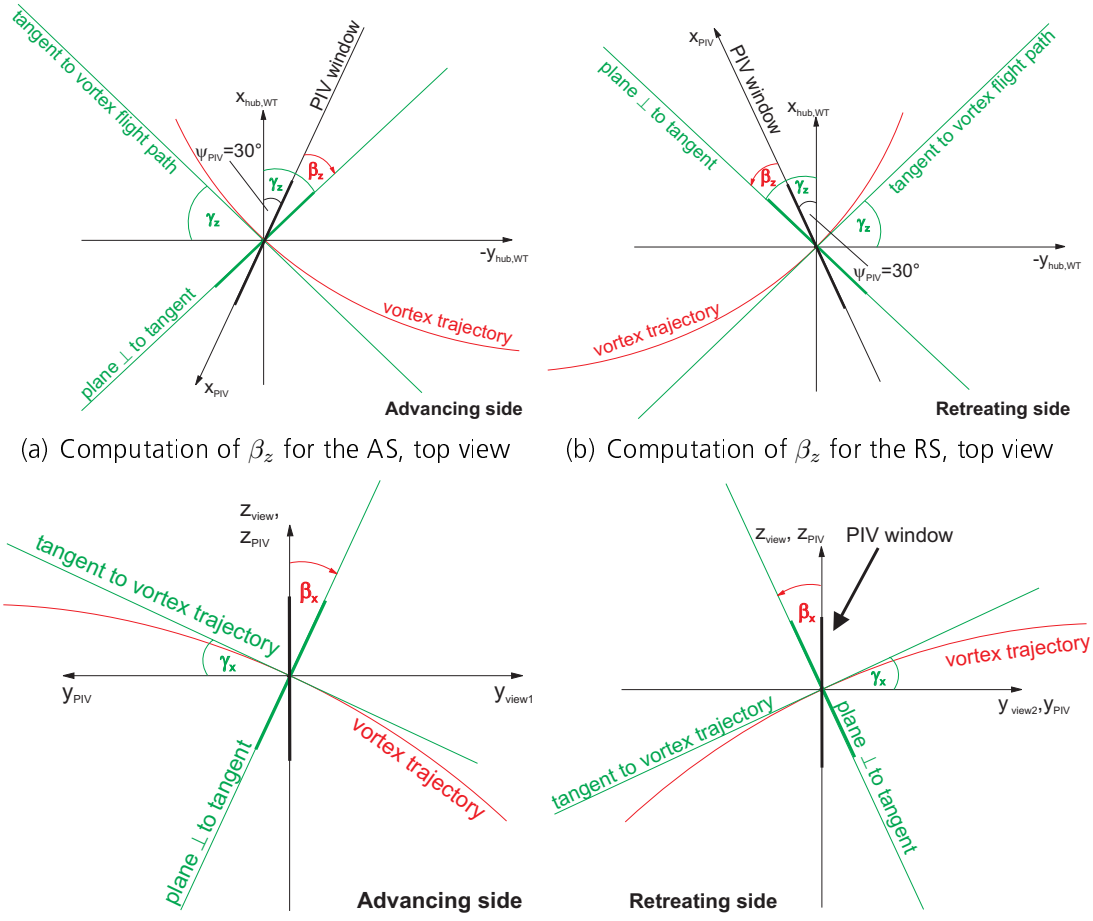

(a) Computation of β_z for the AS, top view

(b) Computation of β_z for the RS, top view

(c) Computation of β_x for the AS, rear view 1

(d) Computation of β_x for the RS, rear view 2

Figure 5: Computation of β_z in the $xy_{hub,WT}$-plane and β_x in the $xz_{view1/2}$-plane

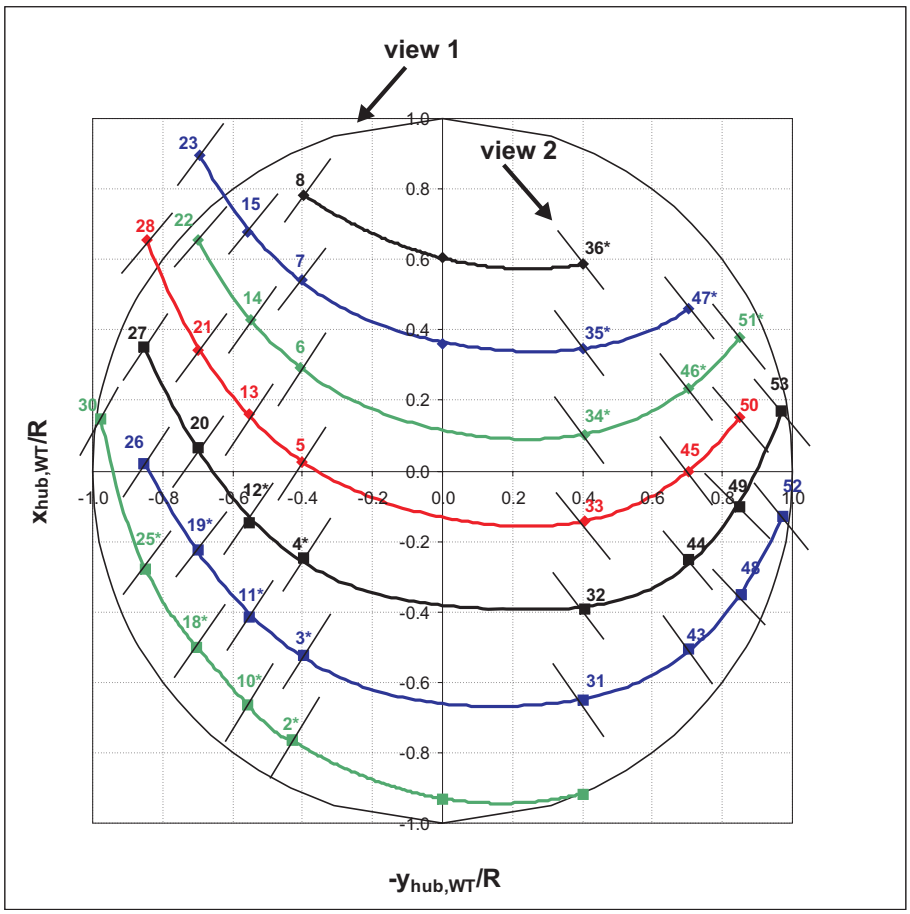

Figure 6: Polynomial approximation of vortex trajectories in the $xy_{hub,WT}$-plane for the computation of β_z, top view, BL case, wind from bottom upwards,
green: $\psi = 200°$, blue: $\psi = 290°$, black: $\psi = 20°$, red: $\psi = 110°$

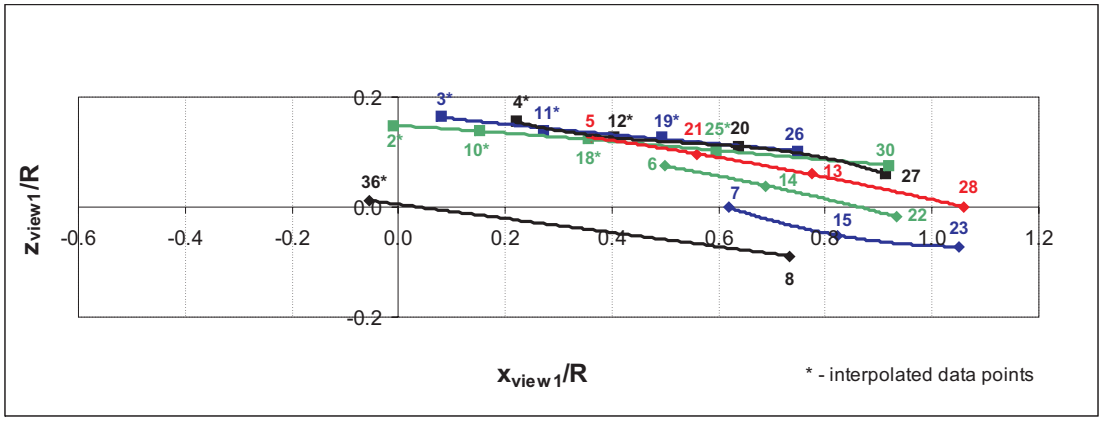

(a) xz_{view1}-plane - AS

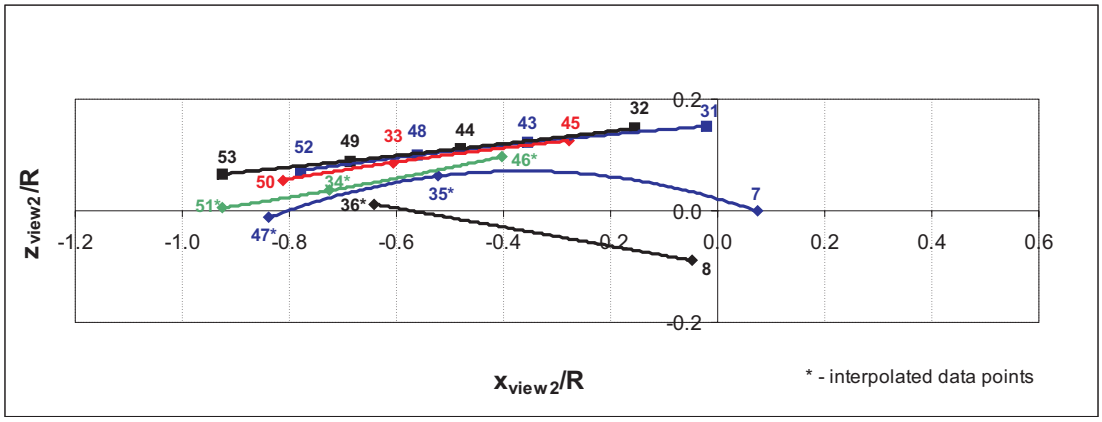

(b) xz_{view2}-plane - RS

Figure 7: Polynomials in the $xz_{view1/2}$-plane for the computation of β_x, BL case

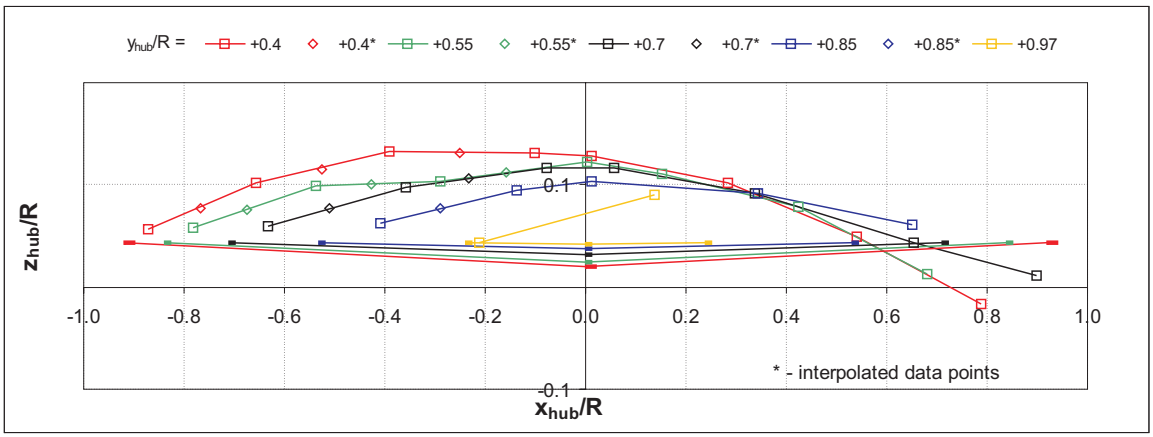

(a) xz_{hub}-plane - AS

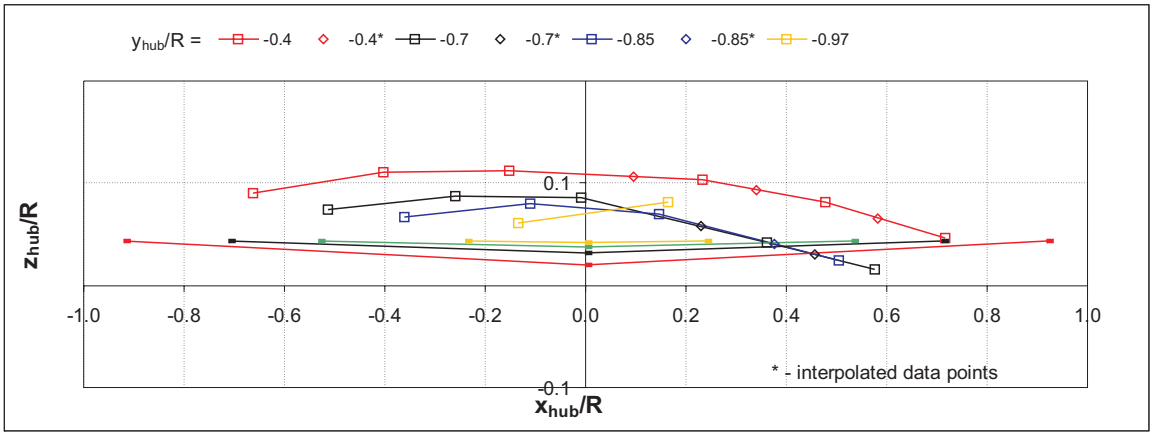

(b) xz_{hub}-plane - RS

Figure 8: Vortex center coordinates in the xz_{hub}-plane, BL case

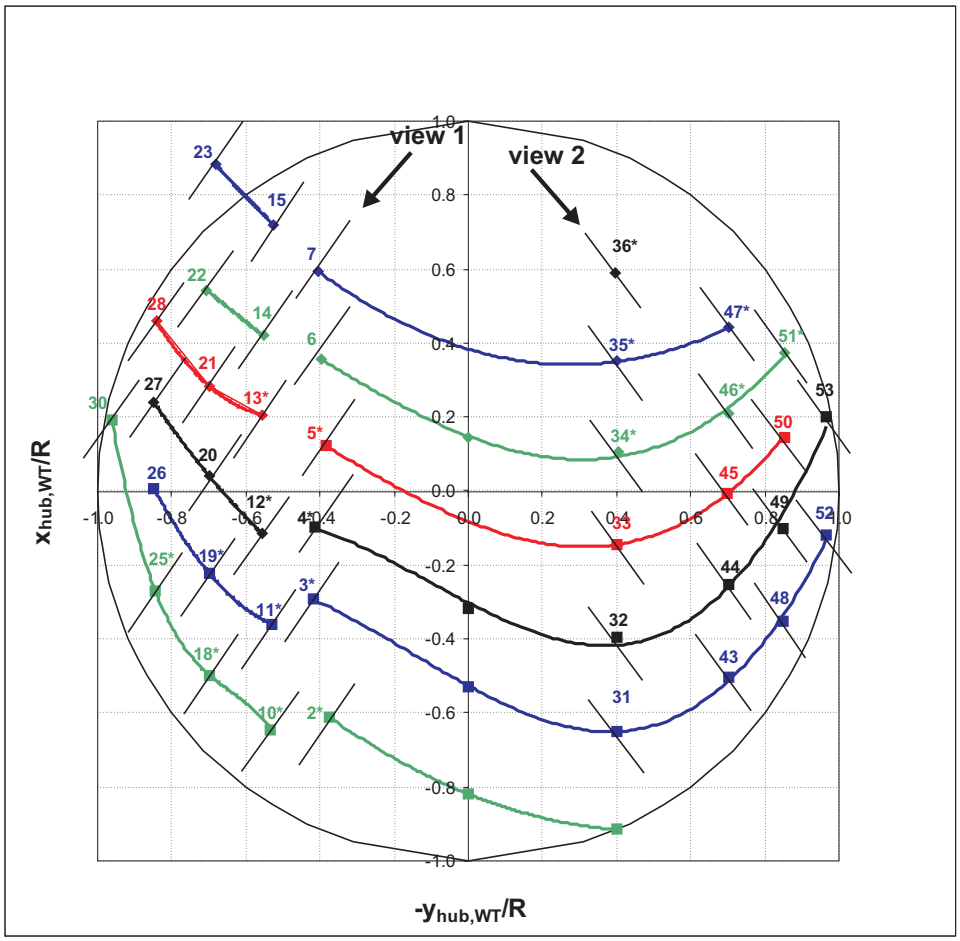

Figure 9: Polynomial approximation of vortex trajectories in the $xy_{hub,WT}$-plane for the computation of β_z, top view, MN case, wind from bottom upwards,
green: $\psi = 200°$, blue: $\psi = 290°$, black: $\psi = 20°$, red: $\psi = 110°$

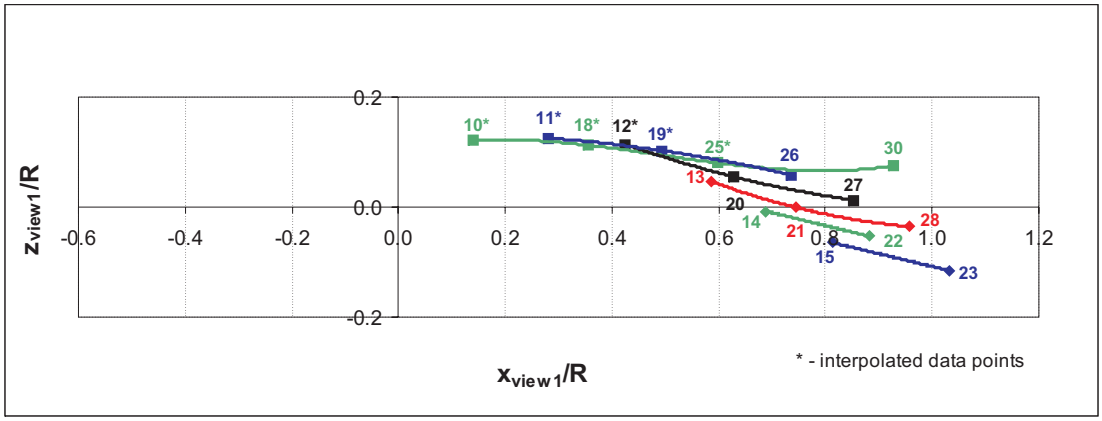

(a) xz_{view1}-plane - AS

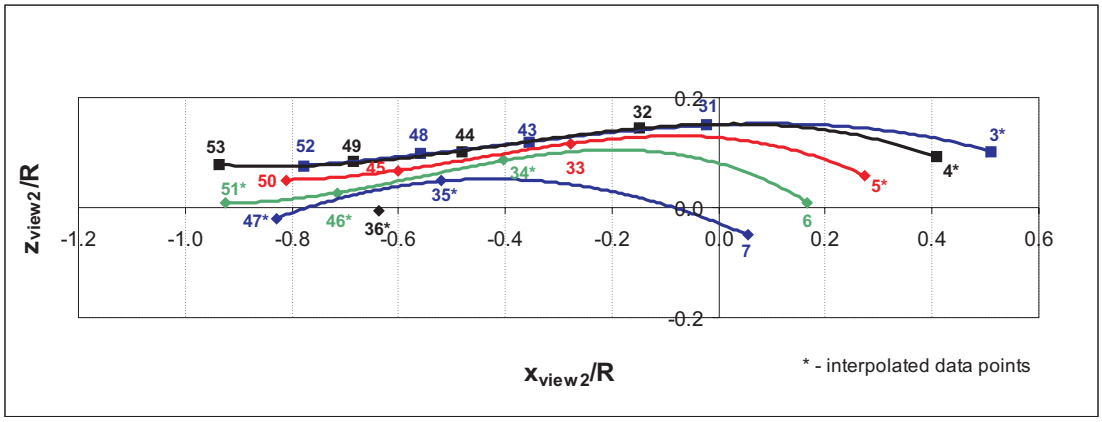

(b) xz_{view2}-plane - RS

Figure 10: Polynomials in the $xz_{view1/2}$-plane for the computation of β_x, MN case

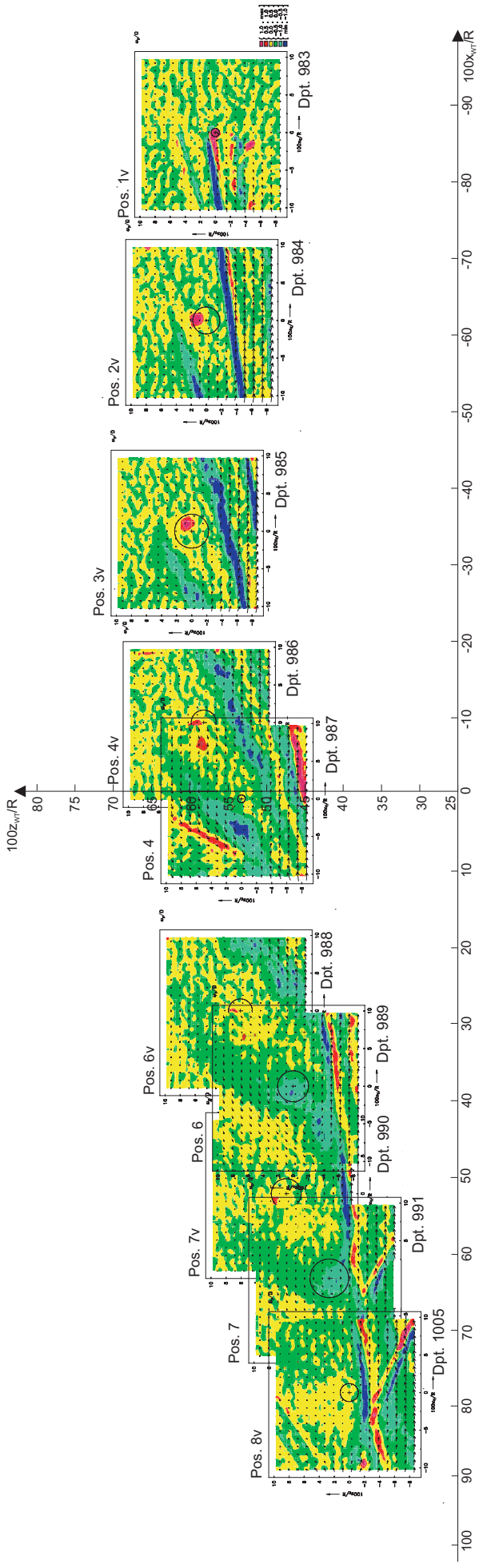

Figure 11: PIV windows for the determination of the vortex centers for analyzing the vortex flight path in the xz_{hub}-plane at $y_{hub} = 0.4R$, MN case, wind from right, hub center at $(-2.5, 0, 45.75)_{WT}$

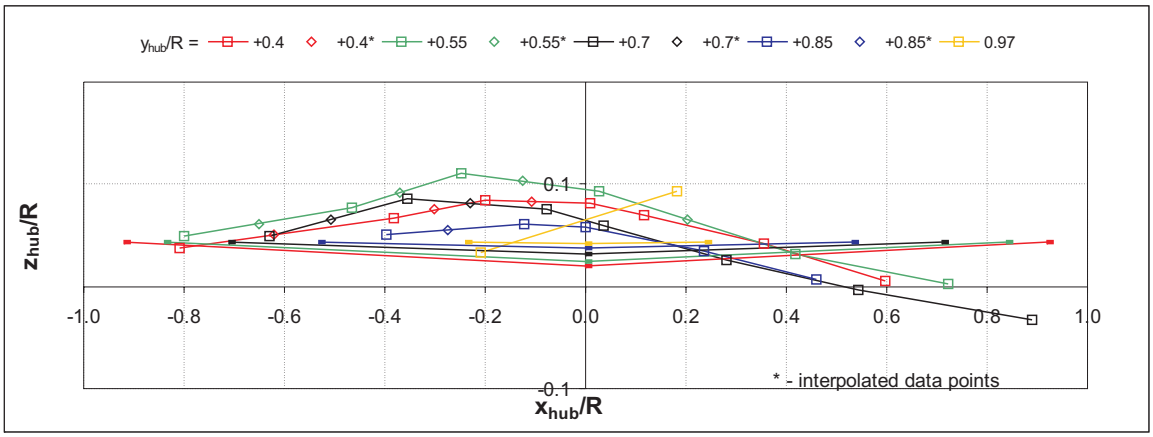

(a) xz_{hub}-plane - AS

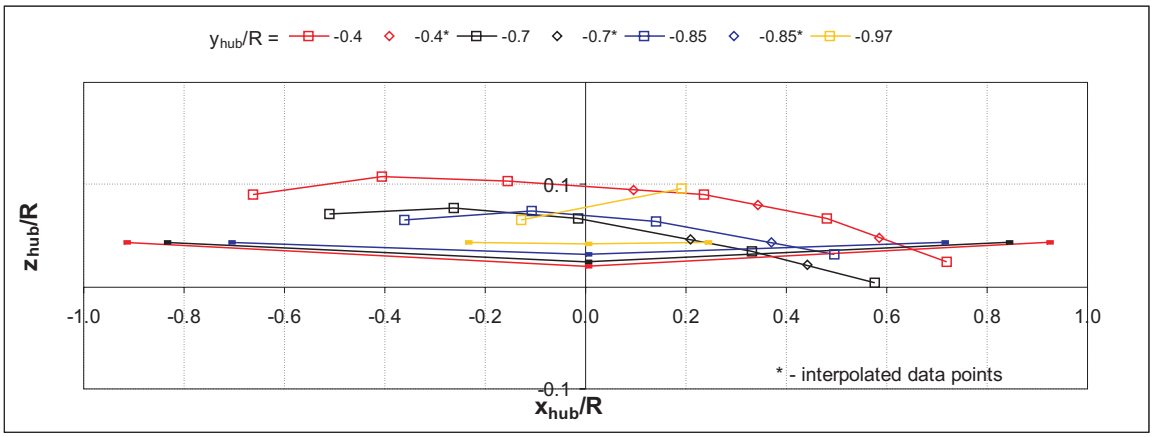

(b) xz_{hub}-plane - RS

Figure 12: Vortex center coordinates in the xz_{hub}-plane, MN case

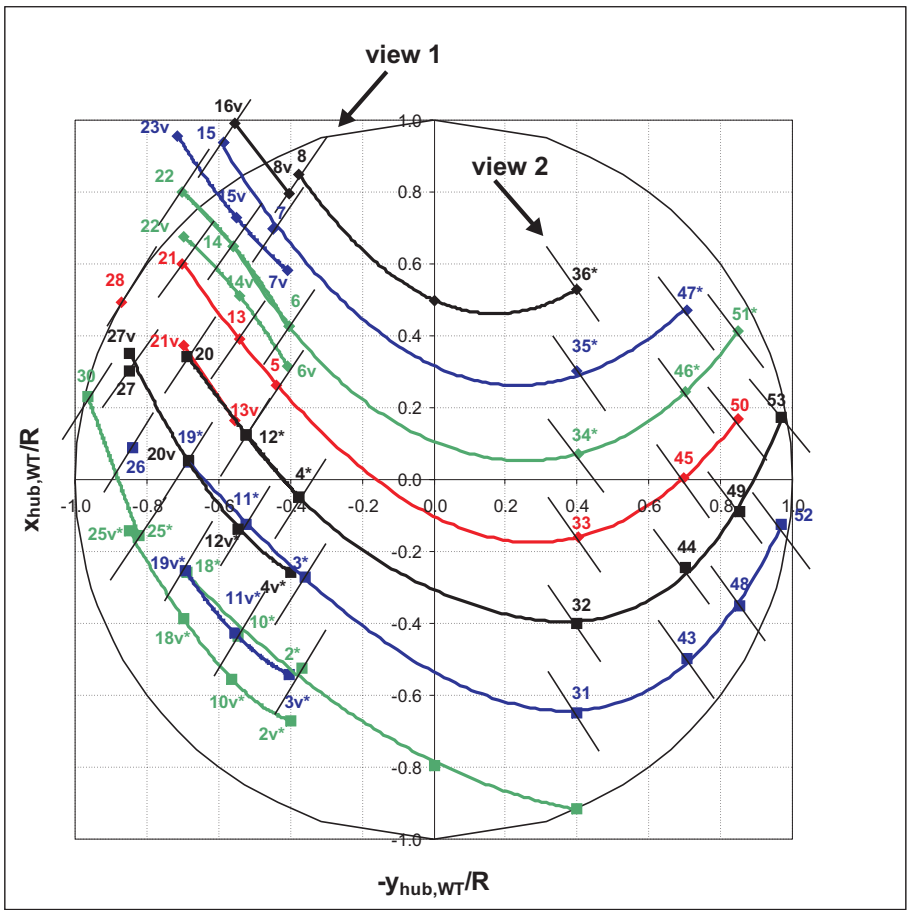

Figure 13: Polynomial approximation of vortex trajectories in the $xy_{hub,WT}$-plane for the computation of β_z, top view, MV case, wind from bottom upwards,
green: $\psi = 200°$, blue: $\psi = 290°$, black: $\psi = 20°$, red: $\psi = 110°$

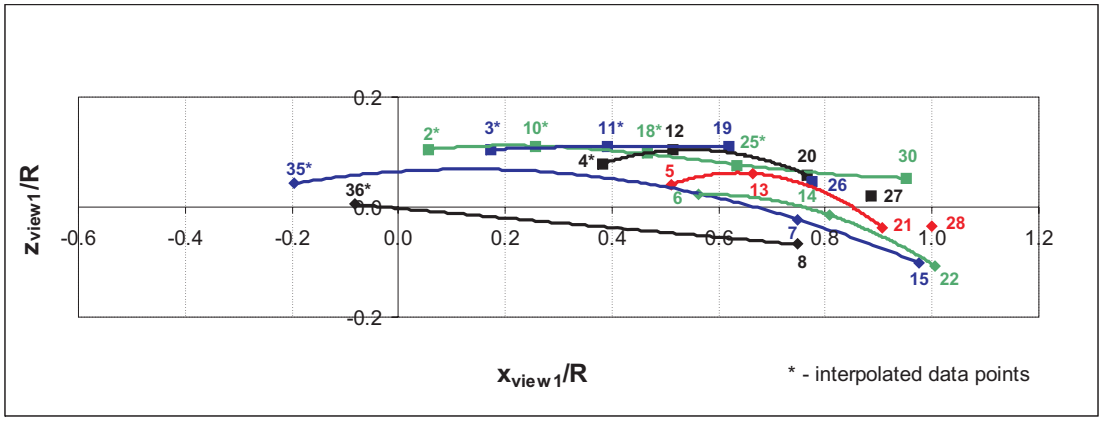

(a) xz_{view1}-plane - AS

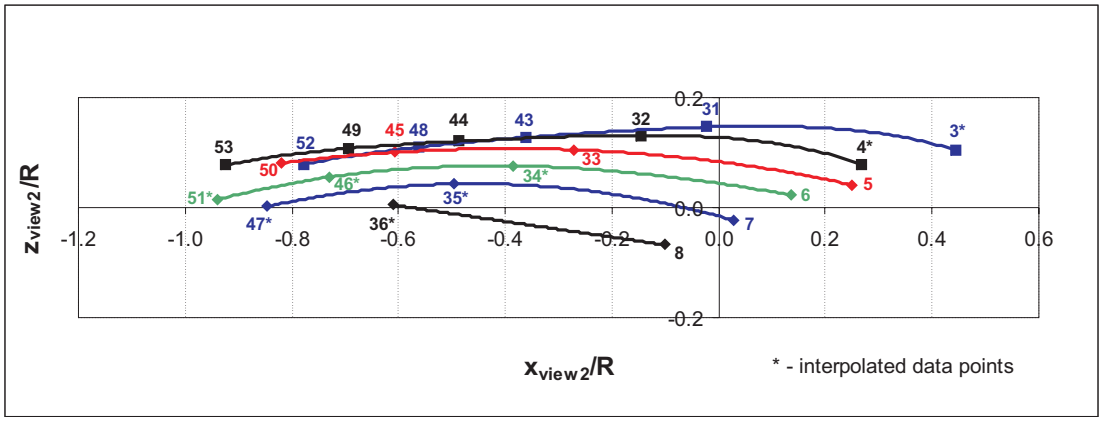

(b) xz_{view2}-plane - RS

Figure 14: Polynomials in the $xz_{view1/2}$-plane for the computation of β_x, MV case

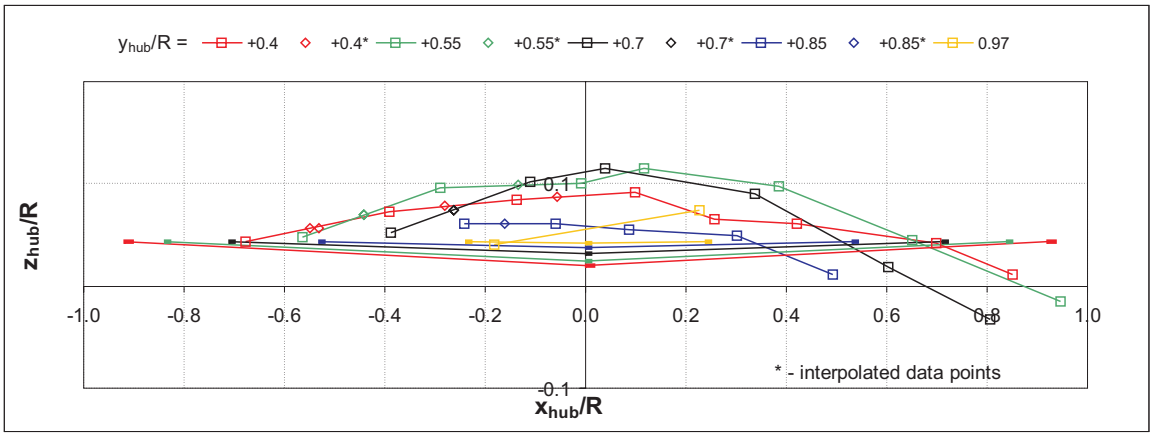

(a) xz_{hub}-plane - AS

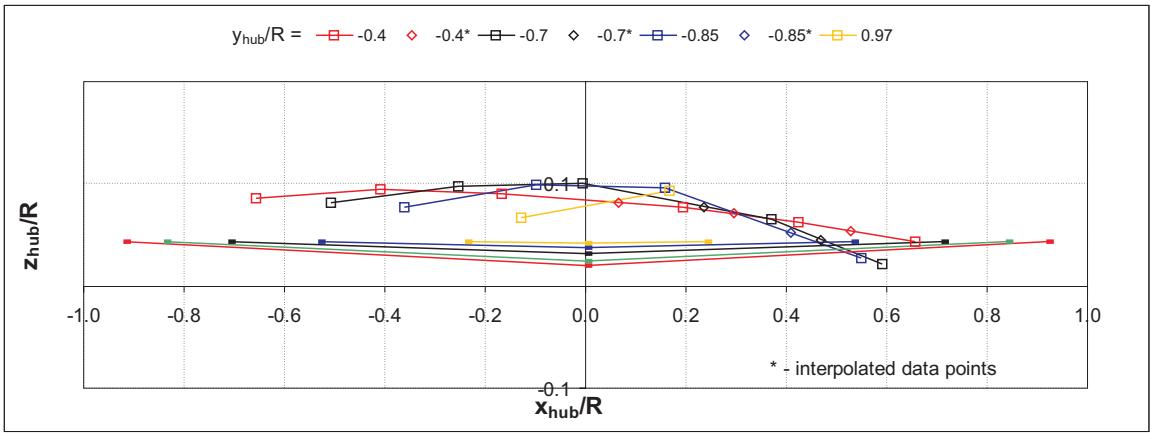

(b) xz_{hub}-lane - RS

Figure 15: Vortex center coordinates in the xz_{hub}-plane, MV case

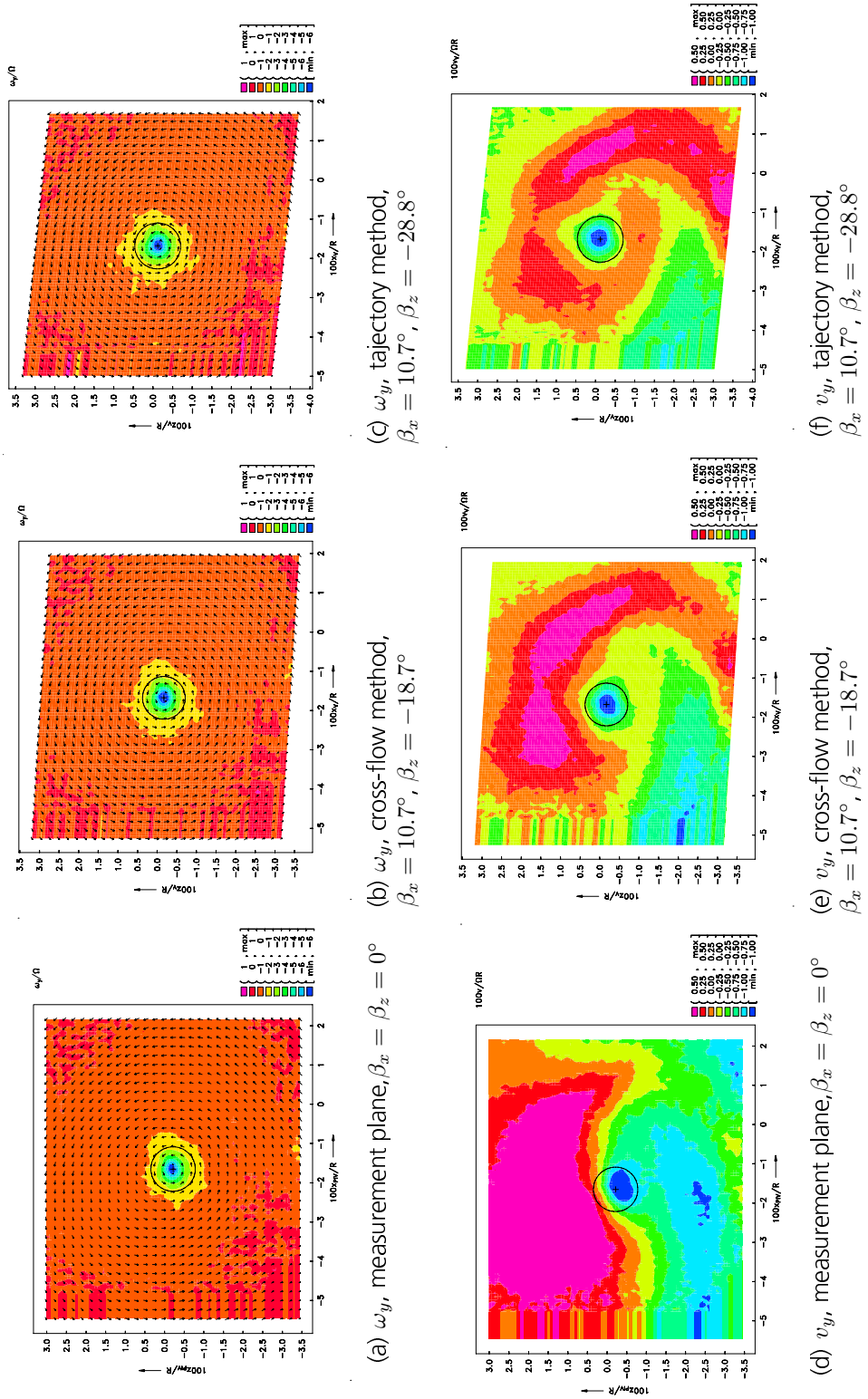

(a) ω_y, measurement plane, $\beta_x = \beta_z = 0°$

(b) ω_y, cross-flow method, $\beta_x = 10.7°$, $\beta_z = -18.7°$

(c) ω_y, tajectory method, $\beta_x = 10.7°$, $\beta_z = -28.8°$

(d) v_y, measurement plane, $\beta_x = \beta_z = 0°$

(e) v_y, cross-flow method, $\beta_x = 10.7°$, $\beta_z = -18.7°$

(f) v_y, tajectory method, $\beta_x = 10.7°$, $\beta_z = -28.8°$

Figure 16: Vorticity and cross-flow velocity computed based on β_x and β_z resulting from cross-flow and trajectory method, BL case, conditional average (method: weighted convolution of parameter λ_2), Pos. 21

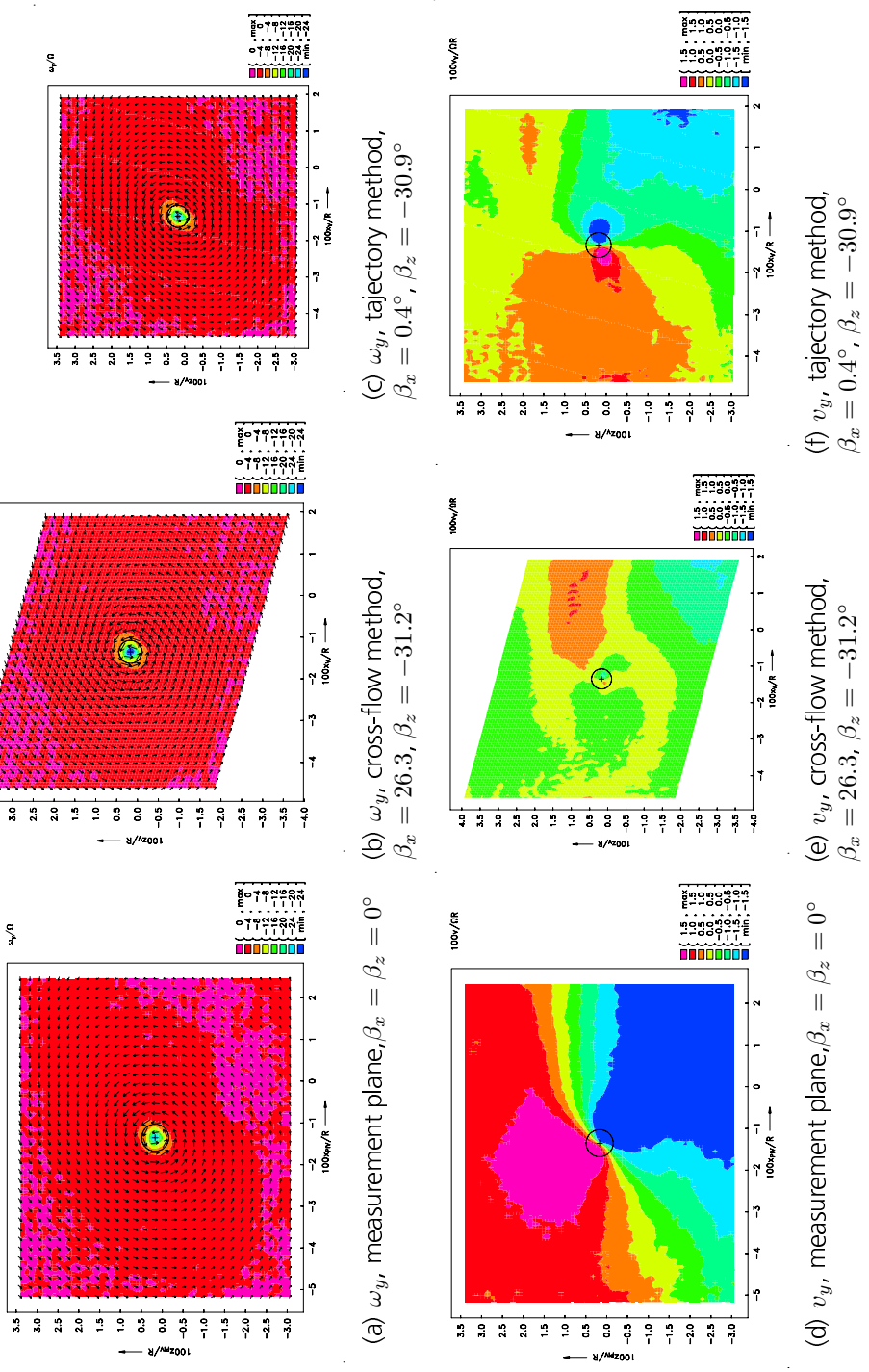

(a) ω_y, measurement plane,$\beta_x = \beta_z = 0°$

(b) ω_y, cross-flow method, $\beta_x = 26.3$, $\beta_z = -31.2°$

(c) ω_y, tajectory method, $\beta_x = 0.4°$, $\beta_z = -30.9°$

(d) v_y, measurement plane,$\beta_x = \beta_z = 0°$

(e) v_y, cross-flow method, $\beta_x = 26.3$, $\beta_z = -31.2°$

(f) v_y, tajectory method, $\beta_x = 0.4°$, $\beta_z = -30.9°$

Figure 17: Vorticity and cross-flow velocity computed based on β_x and β_z resulting from cross-flow and trajectory method, BL case, conditional average (method: weighted convolution of parameter λ_2), Pos. 23

B Tables

Coordinate system	Origin of coordinate system	Index
Wind tunnel CS	Reference point in wind tunnel	WT
PIV measurement CS	In the PIV window	PIV
Rotor hub CS	Center point of the rotor hub	hub, WT
ψ_{view}-rotated rotor hub CS	Center point of rotor hub	$view1/2$
α-rotated rotor hub CS	Center point of the rotor hub	hub

Table 1: Definition of coordinate systems

Blade no.	1	2	3	4
Youngest vortex	black	red	green	blue
1 rev older vortex	black no. 2	red no. 2	green no.2	blue no. 2

Table 2: Blade numbering and associated colors

Advancing Side						Retreating Side					
Position	Dpt	Cross-flow method $\beta_x/°$	Cross-flow method $\beta_z/°$	Trajectory method $\beta_x/°$	Trajectory method $\beta_z/°$	Position	Dpt	Cross-flow method $\beta_x/°$	Cross-flow method $\beta_z/°$	Trajectory method $\beta_x/°$	Trajectory method $\beta_z/°$
green											
30	1052	0.5	-55.4	4.5	-48.8						
blue						blue					
26	1044	-0.2	-29.3	4.4	-32.3	52	1136	6	46.1	7.6	35.8
						48	1114	3.2	21.5	6.6	25.6
						43	1120	0.5	7.8	5.8	9.2
						31	1127	2.5	-11.9	4.3	-19.2
black						black					
27	1045	5.7	-42.0	18.4	-35.8	53	1137	0.6	52.2	5.5	39.3
20	1000	7.2	-21.0	4.6	-27.4	49	1115	4.9	23.7	5.9	29.0
						44	1122	3.2	6.6	6.1	9.9
						32	1128	3.8	-7.0	6.5	-23.3
red no. 2						red no. 2					
28	1047	13.2	-38.7	12.7	-38.4	50	1118	6.7	25.0	9.3	21.7
21	0995	10.7	-18.7	10.7	-28.8	45	1123	5.1	7.3	7.9	9.2
13	0689	1.8	-14.2	9.2	-16.8	33	1129	4.3	-10.4	5.7	-18.7
5	0699	10.2	-3.6	7.7	-4.1						
green no. 2											
22	0998	14.0	-24.9	14.3	-31.2						
14	0688	11.1	-13.3	11.6	-19.7						
6	0698	9.3	4.1	9.5	-7.7						
blue no. 2											
23	0999	26.3	-31.2	0.4	-30.9						
15	0687	9.6	-3.1	9.9	-20.7						
7	0697	12.9	3.3	17.7	-7.4						
black no. 2											
8	0696	0.2	-35.3	7.3	-3.2						

Table 3: Comparison of cross-flow and trajectory method, BL case

Advancing Side			**Retreating Side**		
Position	Delta		Position	Delta	
	$\beta_x/°$	$\beta_z/°$		$\beta_x/°$	$\beta_z/°$
green					
30	4.0	6.6			
blue			blue		
26	4.6	3.0	52	1.2	10.2
			48	3.5	4.1
			43	5.2	1.3
			31	1.8	7.3
black			black		
27	12.7	6.2	53	4.9	12.9
20	2.6	6.4	49	1.0	5.3
			44	3.0	3.4
			32	2.8	16.3
red no. 2			red no. 2		
28	0.5	0.3	50	2.6	3.3
21	0.1	10.1	45	2.9	1.8
13	7.4	2.6	33	1.4	8.4
5	2.4	0.6			
green no. 2					
22	0.3	6.3			
14	0.5	6.3			
6	0.2	11.7			
blue no. 2					
23	25.9	0.3			
15	0.3	17.5			
7	4.8	10.6			
black no. 2					
8	7.1	32.0			

Table 4: Differences of cross-flow and trajectory method, BL case

Advancing Side						Retreating Side					
Position	Dpt	Cross-flow method $\beta_x/°$	$\beta_z/°$	Trajectory method $\beta_x/°$	$\beta_z/°$	Position	Dpt	Cross-flow method $\beta_x/°$	$\beta_z/°$	Trajectory method $\beta_x/°$	$\beta_z/°$
green											
30	0934	-3.8	-49.8	2.7	-49.5						
blue						blue					
26	0938	6.4	-31.8	12.4	-32.2	52	1190	4.6	39.8	3.6	33.8
						48	1189	3.3	19.8	6.2	26.3
						43	1179	1.2	7.0	6.6	12.6
						31	1177	2.9	-9.5	2.7	-27.6
black						black					
27	0939	6.5	-27.2	7.8	-25.5	53	1191	-4.2	43.7	-3.7	36.3
20	0957	13.4	-18.6	13.8	-20.4	49	1187	2.4	21.3	4.6	29.3
						44	1181	3.0	7.8	7.5	16.1
						32	1176	6.1	-1.1	4.8	-25.6
red no. 2						red no. 2					
28	0940	10.0	-30.9	4.8	-27.1	50	1186	6.2	20.0	0.6	20.4
21	0958	20.2	-19.2	13.7	-11.4	45	1182	5.8	5.2	7.7	8.8
						33	1174	9.7	-6.5	7.0	-21.4
green no. 2											
14	0981	25.2	3.0	13.3	-8.9						
6	0989	21.6	-1.2	-61.4	-1.7						
blue no. 2											
23	0964	-1.3	-8.5	13.1	-16.1						
15	0982	37.5	-44.3	13.1	-16.1						
7	0991	36.5	14.6	44.3	-5.4						

Table 5: Comparison of cross-flow and trajectory method, MN case

Advancing Side			**Retreating Side**		
Position	Delta		Position	Delta	
	$\beta_x/^\circ$	$\beta_z/^\circ$		$\beta_x/^\circ$	$\beta_z/^\circ$
green					
30	6.5	0.3			
blue			blue		
26	6.0	0.4	52	1.0	6.0
			48	2.9	6.6
			43	5.3	5.6
			31	0.2	18.1
black			black		
27	1.3	1.7	53	0.5	7.3
20	0.4	1.9	49	2.2	8.0
			44	4.5	8.3
			32	1.3	24.5
red no. 2			red no. 2		
28	5.1	3.8	50	5.6	0.4
21	6.5	7.8	45	1.9	3.7
			33	2.7	14.8
green no. 2					
14	11.9	11.9			
6	83.0	0.5			
blue no. 2					
23	14.4	7.7			
15	24.4	28.2			
7	7.8	20.1			

Table 6: Differences of cross-flow and trajectory method, MN case

Advancing Side						Retreating Side					
Position	Dpt	Cross-flow method $\beta_x/°$	$\beta_z/°$	Trajectory method $\beta_x/°$	$\beta_z/°$	Position	Dpt	Cross-flow method $\beta_x/°$	$\beta_z/°$	Trajectory method $\beta_x/°$	$\beta_z/°$
green											
30	0908	-3.8	-55.1	5.8	-39.9						
blue						blue					
19	0857	22.8	-27.8	0.6	-16.7	52	1147	4.0	41.1	11.3	34.9
						48	1148	5.9	24.0	6.1	26.2
						43	1160	9.5	9.0	4.2	11.0
						31	1162	2.7	-13.0	1.7	-26.6
black						black					
20	0859	9.7	-22.3	24.8	-24.4	53	1145	1.9	52.1	11.3	37.7
						49	1149	5.6	27.7	4.6	28.9
						44	1159	0.8	4.9	2.9	12.7
						32	1163	0.8	-7.3	0.2	-26.7
red no. 2						red no. 2					
21	0862	26.9	3.7	36.4	-24.9	50	1152	6.6	25.7	6.7	21.6
13	0837	7.0	-21.9	3.7	-21.5	45	1157	0.4	8.4	3.6	11.9
						33	1164	-0.1	-9.8	-2.1	-16.7
green no. 2											
14	0839	-2.7	-29.5	18.2	-21.7						
6	0928	17.5	-11.8	-0.9	-29.2						

Table 7: Comparison of cross-flow and trajectory method, MV case

Advancing Side			**Retreating Side**		
Position	Delta		Position	Delta	
	$\beta_x/°$	$\beta_z/°$		$\beta_x/°$	$\beta_z/°$
green					
30	9.6	15.2			
blue			blue		
19	22.1	11.1	52	7.3	6.1
			48	0.1	2.2
			43	5.3	2.0
			31	1.0	13.7
black			black		
20	15.1	2.0	53	9.4	14.4
			49	0.9	1.2
			44	2.1	7.9
			32	0.6	19.4
red no. 2			red no. 2		
21	9.6	28.7	50	0.1	4.1
13	3.3	0.4	45	3.2	3.5
			33	2.1	6.9
green no. 2					
14	20.9	7.8			
6	18.4	17.4			

Table 8: Differences of cross-flow and trajectory method, MV case

$xy_{hub,WT}$-plane	**Advancing Side**	**Retreating Side**
green	$x = 24.847y^4 + 63.161y^3 + 60.228y^2 + 24.391y + 2.7583$	$x = 0.5758y^2 - 0.1646y - 0.9433$
blue	$x = 0.2132y^5 + 0.4104y^4 - 0.3117y^3 + 0.3895y^2 - 0.1037y - 0.6609$	$x = 0.2132y^5 + 0.4104y^4 - 0.3117y^3 + 0.3895y^2 - 0.1037y - 0.6609$
black	$x = 0.2674y^5 + 0.595y^4 - 0.4018y^3 + 0.278y^2 - 0.1032y - 0.3819$	$x = 0.2674y^5 + 0.595y^4 - 0.4018y^3 + 0.278y^2 - 0.1032y - 0.3819$
red no.2	$x = -0.1373y^5 + 0.5231y^4 - 0.0424y^3 + 0.3721y^2 - 0.2014y - 0.1323$	$x = -0.1373y^5 + 0.5231y^4 - 0.0424y^3 + 0.3721y^2 - 0.2014y - 0.1323$
green no. 2	$x = -0.0797y^5 + 0.5101y^4 - 0.1599y^3 + 0.4181y^2 - 0.2038y + 0.1155$	$x = -0.0797y^5 + 0.5101y^4 - 0.1599y^3 + 0.4181y^2 - 0.2038y + 0.1155$
blue no. 2	$x = 0.5175y^4 - 0.2528y^3 + 0.3898y^2 - 0.1955y + 0.3653$	$x = 0.5175y^4 - 0.2528y^3 + 0.3898y^2 - 0.1955y + 0.3653$
black no. 2	$x = 0.5088y^2 - 0.2479y + 0.6038$	$x = 0.5088y^2 - 0.2479y + 0.6038$
$xz_{view1/2}$-plane		
green	$z = 0.0228x^3 - 0.0426x^2 - 0.0579x + 0.1479$	$-$
blue	$z = 0.0198x^2 - 0.1066x + 0.1714$	$z = -0.0377x^2 + 0.0741x + 0.1531$
black	$z = -0.6421x^3 + 1.0264x^2 - 0.6052x + 0.2455$	$z = 0.0114x^2 + 0.1182x + 0.1655$
red no.2	$z = -0.0634x^2 - 0.0902x + 0.1672$	$z = -0.0604x^2 + 0.0657x + 0.1485$
green no. 2	$z = -0.1013x^2 - 0.0662x + 0.1328$	$z = 0.0646x^2 + 0.2616x + 0.1921$
blue no. 2	$z = 0.3638x^2 - 0.7706x + 0.3366$	$z = -0.3723x^2 - 0.2718x + 0.0217$
black no. 2	$z = -0.1278x + 0.0048$	$z = -0.1698x - 0.0971$

Table 9: Polynomial equations, BL case

$xy_{hub,WT}$-plane	Advancing Side	Retreating Side
green	$x = -15.474y^3 - 29.872y^2 - 19.958y - 5.1457$	$x = 0.4036y^2 - 0.4027y - 0.8191$
blue	$x = 2.312y^2 + 2.0322y + 0.0684$	$x = 0.695y^3 + 0.3181y^2 - 0.5463y - 0.527$
black	$x = 0.8134y^2 - 0.0719y - 0.4069$	$x = 0.818y^3 + 0.2537y^2 - 0.519y - 0.302$
red no. 2	$x = 2.3741y^2 + 2.4419y + 0.8307$	$x = 0.375y^3 + 0.4696y^2 - 0.4036y - 0.0823$
green no. 2	$x = -0.806y - 0.0264$	$x = 0.3123y^3 + 0.481y^2 - 0.3816y + 0.1481$
blue no. 2	$x = -1.0395y + 0.1722$	$x = 0.5416y^2 - 0.3001y + 0.3836$
black no. 2	$-$	$-$
$xz_{view1/2}$-plane		
green	$z = 0.5157x^3 - 0.7637x^2 + 0.2364x + 0.1017$	$-$
blue	$z = -0.1652x^2 + 0.0215x + 0.1323$	$z == -0.1483x^3 - 0.1865x^2 + 0.0393x + 0.1507$
black	$z = 0.2349x^2 - 0.5368x + 0.2996$	$z = -0.2433x^3 - 0.2964x^2 + 0.0148x + 0.152$
red no.2	$z = 0.362x^2 - 0.7794x + 0.379$	$z = -0.3918x^3 - 0.531x^2 - 0.0785x + 0.1271$
green no. 2	$z = -0.2365x + 0.1555$	$z = -0.5084x^3 - 0.8474x^2 - 0.2713x + 0.0805$
blue no. 2	$z = -0.2325x + 0.1245$	$z = -0.4406x^2 - 0.3764x - 0.0284$
black no. 2	$-$	$-$

Table 10: Polynomial equations, MN case

$xy_{hub,WT}$-plane	**Advancing Side**	**Retreating Side**
green	$x = -2.7259y - 2.3985$	$x = 0.0642y^3 + 0.4144y^2 - 0.5006y - 0.7871$
blue	$x = 0.1318y^5 + 0.1212y^4 + 0.192y^3 + 0.5723y^2 - 0.5393y - 0.5348$	$x = 0.1318y^5 + 0.1212y^4 + 0.192y^3 + 0.5723y^2 - 0.5393y - 0.5348$
black	$x = 0.4129y^2 - 0.8249y - 0.4171$	$x = 0.6284y^4 - 0.1394y^3 + 0.5047y^2 - 0.4397y - 0.3066$
red no.2	$x = 0.1653y^3 + 0.8297y^2 - 0.5065y - 0.1018$	$x = 0.1653y^3 + 0.8297y^2 - 0.5065y - 0.1018$
green no. 2	$x = -1.381y^2 - 2.7839y - 0.473$	$x = 0.3003y^4 - 0.1562y^3 + 0.8296y^2 - 0.4125y + 0.1055$
blue no. 2	$x = 0.9813y^2 - 0.4614y + 0.3166$	$x = 0.9813y^2 - 0.4614y + 0.3166$
black no. 2	$x = 1.296y^2 - 0.444y + 0.5$	$x = 1.296y^2 - 0.444y + 0.5$
$xz_{view1/2}$-plane		
green	$z = 0.2573x^3 - 0.4547x^2 + 0.1534x + 0.0974$	$-$
blue	$z = -0.0583x^2 + 0.06x + 0.0961$	$z = -0.1863x^4 - 0.2135x^3 - 0.1356x^2 + 0.0243x + 0.1471$
black	$z = -0.948x^2 + 1.0348x - 0.178$	$z = -0.24x^4 - 0.416x^3 - 0.3075x^2 - 0.0645x + 0.1275$
red no.2	$z = -1.3451x^2 + 1.7101x - 0.4812$	$z = -0.0185x^3 - 0.1702x^2 - 0.1248x + 0.0833$
green no. 2	$z = -0.7193x^2 + 0.836x - 0.2201$	$z = 0.0549x^3 - 0.1326x^2 - 0.1413x + 0.0442$
blue no. 2	$z = -0.2404x^2 + 0.0636x + 0.0647$	$z = -0.2783x^2 - 0.2558x - 0.0154$
black no. 2	$z = -0.0875x - 0.0024$	$z = -0.142x - 0.0821$

Table 11: Polynomial equations, MV case

This page is to be thrown away

Figure 17: This page is to be thrown away

This page is to be thrown away

Table 11: This page is to be thrown away